DICUAM 2022, 22-24 March 2022

Aerodynamic installation effects on the sound emissions of a drone in hover

Alessandro Zarri[1,2], Edoardo Dell'Erba[1], Wim Munters[1] and Christophe Schram[1]

[1]Environmental and Applied Fluid Dynamics Department, von Karman Institute for Fluid Dynamics, Chaussée de Waterloo 72, 1640 Rhode-St-Genèse, Belgium
[2]*alessandro.zarri42@gmail.com*

Abstract

Noise emitted by unmanned aerial vehicles such as drones and soon Urban Air Mobility vehicles is becoming a concern in metropolitan areas. It involves complex aerodynamic and acoustic installation effects which need a deeper understanding to reach quieter designs. In this work, focused on tonal noise emissions, we have developed a hybrid methodology that combines unsteady Reynolds-Averaged Navier-Stokes simulations with a computational aeroacoustics approach based on the Ffowcs Williams and Hawkings' analogy. The methodology has been validated by comparing the predicted tones with acoustic measurements from the literature. Two aeroacoustic installation effects have been investigated in hover flight conditions: tip-on-tip and tip-on-strut interactions. We have established that these interactions are dictating the tonal noise emissions. In particular, the tip-on-tip interaction induces a maximum thrust variation of 7% compared to the average value and a loss in the aerodynamic performances of 7%. The interaction with the supporting struts induces additional periodic loads on the blades for frequencies that are multiples of the blade passing frequency. The sound directivity maps in the near field are found to be relevantly altered, up to 30 dB differences, when comparing the sound emission including or not the drone body.

1 Introduction

The world of aeronautics has been characterized in recent years by the advent of Unmanned Aerial Vehicles (UAVs), commonly known as drones [4]. Initially used for recreational or military purposes only, UAVs now have numerous applications [2] ranging from high-definition aerial photos to inspecting at-risk building constructions [16, 14]. With the increasing use and popularity of drones, one of the critical consequences is the concern associated with their noise emissions, especially in urban environments [26, 5]. Drones acoustic radiations, similar to a loud buzzing sound, are also perceived as highly annoying and therefore there is interest in studying their origin, understanding their generation mechanisms, and reducing their unpleasant effects. This is also in order to standardize the measurements made on drones and their certification procedures. Among the various small-sized aerial vehicle concepts proposed in recent years, those with rotary wings represent the vast majority [15] since they have the advantage of taking off and landing vertically and present a high level of maneuverability. UAVs typically use propellers to fly, each one controlled by an electric motor, radiating discrete tonal peaks at the Blade Passing Frequency (BPF) and its multiples (harmonics) [10]. Broadband sound components also exist [20], which are due to the random lift variations induced by the interaction between blade edges and turbulence [29]. However, this work focuses only on the tonal sound, since it is perceived by the human ear as more annoying [25].

Ffowcs Williams and Hawkings' derivations [9] are the mathematical backgrounds of rotational machinery acoustics, including the case of UAV propellers. According to those, one can identify sound generating mechanisms intrinsically linked to the aerodynamic performances, i.e., thickness noise and steady-loading noise. The former corresponds to monopole-like sources that depend on the inner volume of the blades and it is known once the blade kinematics is prescribed. The latter is depending on the average of the blade forces, particularly the thrust, that radiates through a dipolar term because of the rotating motion acceleration. Nevertheless, as discussed for instance by Goldstein [10] for subsonic rotating thin blades, the dominant sound mechanisms are due to the environment in which the propellers operate, the so-called installation effects that yield unsteady-loading noise.

The installation effects can be defined as the sound emission differences from an isolated propeller to the same propeller once installed on the aircraft. There are aerodynamic installation effects, caused by non-axisymmetric flows ingested by the propeller once installed in its operational environment. Non-uniform inflow conditions cause periodic perturbations on the blades, leading to periodic loads that radiate tonal noise. These perturbations have typically two origins for drones in hover: the potential interaction between the propellers and their supporting struts [31], and rotor-on-rotor interactions [8]. Hence, both sound mechanisms are induced by the proximity of the propeller to other parts of the drone, inducing relevant unsteady fluctuations of thrust that radiate noise. As these mechanisms are dominant, whichever prediction strategy aimed at describing tonal emissions from drones must take them into account. In addition to aerodynamic installations, there are acoustic installations [19]. These are due to the scattering of sound waves that, once produced by the generation mechanisms discussed above, interact with other parts of the drone such as the fuselage. The acoustic wave reflections might induce substantial amplification or shielding effects that change the directivity of the UAV's overall radiation. Their characterization will be the object of future publications. The main objective of the present work is to describe the effect of the aerodynamic interactions on the flow when compared to an isolated-propeller case. Moreover, we are interested in understanding whether both the effects of the supporting struts and the interaction between rotors are relevant in the generation of unsteady loading sources. The aeroacoustic sources are calculated by solving a Computational Fluid Dynamics (CFD) simulation that takes into account the relevant unsteady effects of the flow developing around the drone. Once obtained, these aerodynamic forces are used as input to a commercial numerical solver to obtain the free-field sound emissions. Although few works on drone aerodynamics are available in the literature, one can find some relevant ones employing high-order methods able to simultaneously compute the flow and sound fields. See for example the work of Casalino *et al.* [6] solving the Lattice Boltzmann equations combined with a Very-Large-Eddy Simulation model. Another high-order Delayed Detached Eddy Simulation (DDES) approach [24], this time solving compressible Navier-Stokes equations, was adopted by Yoon *et al.* [27] exploiting the Pleiades supercomputer at NASA Advanced Supercomputing Division to obtain the aerodynamic solution achieved on a very fine grid of 225 million cells. While the numerical works mentioned above can achieve a higher degree of accuracy, the additional goal in this work is to define a relatively low-order methodology that can be used in future optimization cycles during the early development phase of new drone concepts, similar to what is commonly done, for example, in the automotive field [30].

2 CFD modeling

In this paper, the analysis is based on the commercial quadcopter DJI Phantom 3 Advanced [1]. The simplified fuselage geometry, adopted in the numerical simulations discussed below, was made available by NASA Ames Research Center, USA. It is visible in Figure 1(a): the main simplification consists in the fact that the camera is removed to reduce the additional computational cost, related to its discretization. Yet, it includes the four supporting arms attached to a central body and the landing gear. A further simplification consists in the absence of solid parts representing the brushless motors. This is because the gap between the center of the propeller and the supporting strut is quite small and therefore does not influence the overall flow features. The propeller used is a DJI 9450, with an average chord of approximately $0.025\,\mathrm{m}$ and a rotor diameter $D = 0.239\,\mathrm{m}$. Its clockwise version is obtained by mirroring the CAD in the spanwise direction. The setup used in this work includes four propellers, whose relative initial positions are shown in Figure 1(a). The uRANS computations are carried out with the commercial solver Simcenter STAR-CCM+ Version 16.04. To initialize the simulations, a steady moving reference frame is used in a cylindrical refinement region of diameter $L = 1.2D$ around the rotating propellers (see for instance [30]). For the subsequent unsteady simulation, these regions are replaced by sliding-mesh ones. The foregoing length scale L is further used as the base size for the construction of the entire bullet-shaped computational domain shown in Figure 1(b). It reaches a width of $20L$ in the rotor plane, a radius of $10L$ in the spherical upstream part, and a length of $40L$ in the axial downstream direction, assuring negligible interactions between rotating parts and domain boundaries [28]. The boundary conditions are chosen to simulate hovering. For that, the stagnation-inlet condition is imposed everywhere but at the bottom of the bullet-shaped domain, where we used a pressure-outlet condition to allow the flow to exit the domain. The rotational speed of the propellers is fixed to $6000\ \mathrm{rpm}$, corresponding to a rotational frequency of $\Omega = 100\,\mathrm{Hz}$. This leads to an incompressible subsonic flow regime with a Reynolds number of $1.25 \cdot 10^5$ based on tip velocity and average chord length. Time integration is performed using second-order implicit second-order implicit backward differentiation formula, in which the time step $\Delta t = 8.33 \cdot 10^{-5}\ \mathrm{s}$ is chosen to have 3° of rotating mesh displacement per Δt. The k–ω SST turbulence model [17] is adopted, justified by its satisfactory performance in recent UAV studies employing similar numerics (see, e.g., [7, 11]). The simulation grid is built from polyhedral cells, mostly clustered

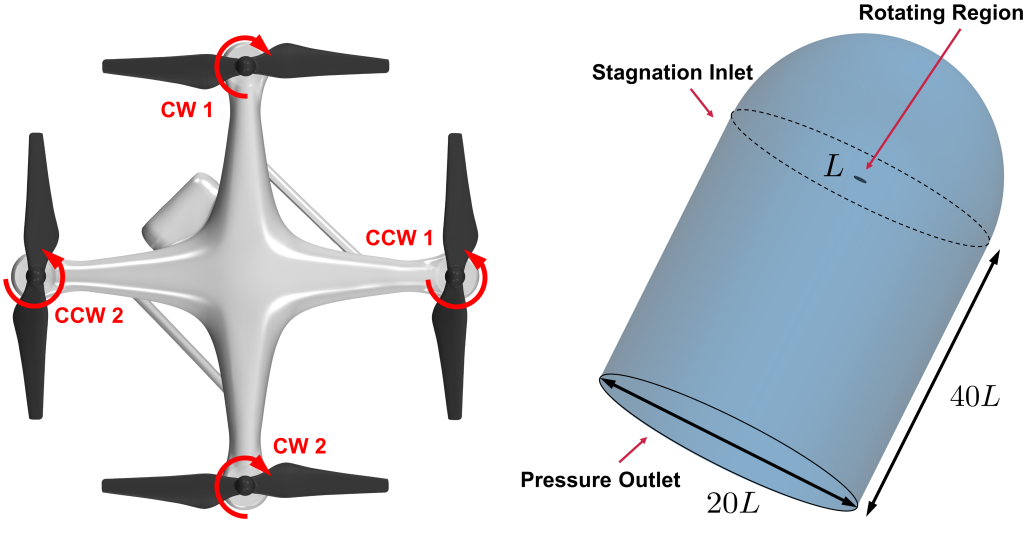

(a) (b)

Figure 1: (a) DJI Phantom 3 Advanced geometry used in this work with the initial conditions of the four propellers: two rotating clockwise (CW1 and CW2), two rotating counterclockwise (CCW1 and CCW2). (b) Bullet-shaped computational domain: the width $L = 1.2D$ serves as the base size for the construction of the entire domain.

around propellers and fuselage (see a close-up view of the mesh on the drone body and propeller in Figure 2(a)). Using established correlations for flat plates [22], a boundary-layer thickness of about $1\,\mathrm{mm}$ is expected at the rotor blade trailing edge. The boundary layer is discretized by 20 prism layers, in order to achieve a wall resolution at $y^+ < 5$ viscous units everywhere. Away from the boundary layers, the global grid resolution is chosen based on a grid convergence validation study by comparing simulated thrust values to experimental measurements. All the parameters that define the grid, except the thickness of the boundary layer and the number of prism layers inside it, are expressed as relative percentages of the characteristic dimension L. Therefore it is possible to vary this dimension to progressively refine the grid. This is carried out for both a single isolated propeller (grid 1) and the quadcopter geometry (grid 2) compared with the experimental results measured by Russell *et al.* [21]. Grid 1 comprises approximately 5 million polyhedral cells with a percentage difference from the measured thrust value of 5.7%, whereas grid 2 contains 8.65 million cells and differs from the thrust measured value of 1.4%. The validated uRANS simulation setup is then used in three configurations, i.e., one with the single isolated propeller (grid 1), one with the quadcopter geometry including four propellers and the fuselage (grid 2), and one with only

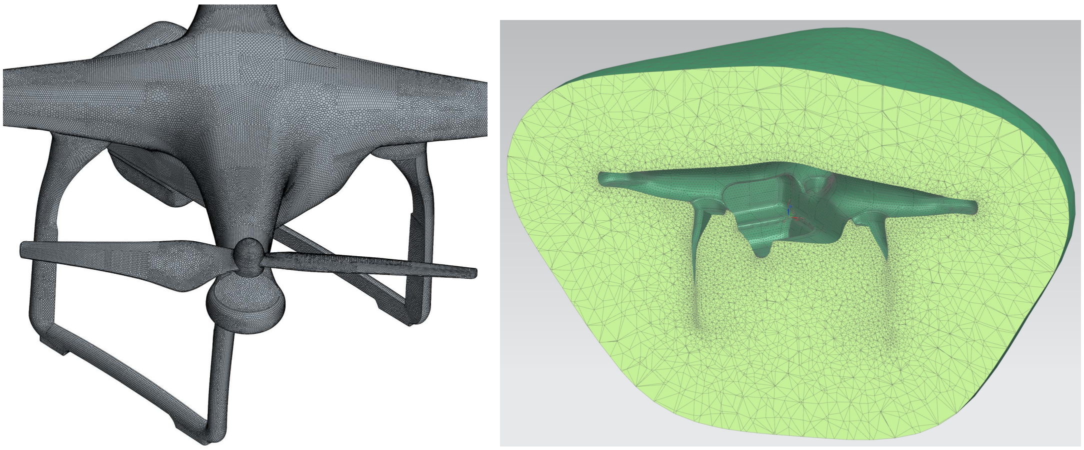

(a) (b)

Figure 2: (a) Polyhedral mesh used for the unsteady RANS depicted with a view over the drone body. (b) Finite element mesh calculated with tetrahedral elements built around the drone fuselage.

four propellers (grid 2, but with fuselage refinement regions omitted).

3 Acoustic modeling

This section describes the acoustic modeling approach used to obtain the results shown below, exploiting the CFD simulation discussed in Section 2. Data of the aerodynamic forces along the propeller blades are extracted from the uRANS simulation in the form of CFD General Notation System (CGNS) files. These are used as input into the commercial solver Simcenter Nastran. Here, a frequency domain formulation capable of computing discrete tones at BPF and harmonics is available. This approach is commonly referred to as source mode and is an equivalent reconstruction of rotating dipolar sources using fixed dipoles; the exact mathematical derivation is available in [18]. The dipole source strengths are obtained by integrating the transient pressure field over acoustically-compact blade segments. Three components of force per segment are considered respectively along the radial, azimuthal, and axial directions. The solver reconstructs the rotating source as equivalent stationary components in the frequency domain. Firstly, the rotating transient source terms are projected to high-order degrees-of-freedom of the finite element problem during their trajectory. Then, they are converted to the frequency domain *via* Fourier Transform (more details are given in Simcenter 3D User's Guide [23]). A Finite Element Method (FEM) mesh is built with elements that need to discretize well all geometrical features of the fuselage: in this case, a superficial element size of $3\,\mathrm{mm}$ has been used with linear triangular elements, whereas tetrahedral elements are used to fill the volume shown in Figure 2(b). Typically, using the linear tetrahedral elements in the propagation volume, the finite element size must be less than $1/6$ of the smallest acoustic wavelength of interest. Thanks to the adaptive order formulation employed, this constraint can be relaxed in the mesh generation. The propagation solver automatically increases the order of the element in case the mesh discretization is too coarse for the given frequency hence wavelength. Non-reflective boundary conditions envelop the acoustic finite element domain, defined with Automatically Matched Layer boundaries [3]. This allows the listeners to be defined also outside the meshed domain. The mesh that includes the fuselage is used only in Section 4.1, in order to validate the acoustic results against the experimental ones. Nevertheless, a similar finite element grid that does not include the fuselage geometry is considered for the subsequent analysis to study the free-field propagation of the four propellers. Indeed, the quantification of the scattering effects of the fuselage will be the object of future publications. On the contrary, the interest is here to quantify the aerodynamic installation effects of the fuselage when this is considered or not in the uRANS simulation.

4 Results

The validation of the proposed acoustic prediction methodology is presented first in this section, followed by the aerodynamic installation effects, specifically the tip-on-tip interaction and the tip-on-strut interaction.

4.1 Validation of the acoustic prediction

In Figure 3(a), the schematic shows the spatial location of the microphone used by Intaratep *et al.* [13] to measure the SPL of a DJI Phantom 2 in hover. The microphone was positioned in the plane $(xz)(y=0)$, forming an angle of $\theta = 130°$ with the z-axis, at a distance $r = 6.32D$ from the center of the quadcopter. These measurements are used to validate the hybrid uRANS+FEM approach described above. This is acceptable as their model utilizes the same propellers as the DJI Phantom 3 Advanced and has an almost identical fuselage. A satisfactory agreement is reached for all tones up to the fourth BPF, as visible in Figure 3(b), showing deviations with respect to the measurements always below $3.5\,\mathrm{dB}$. The simulation used to validate the numerical approach includes the scattering effects due to the presence of the fuselage. Nevertheless, in the subsequent sections, those effects will not be considered as the focus is here put on the quantification of the aerodynamic installation effects.

In Figure 7(a) a hemisphere is shown on the downstream side of the quadcopter, at $r = 1.1D$ from the center of it (position of the center given in Figure 3(a)). We calculate L_p on the hemisphere through the FEM-based approach discussed in Section 3. This is achieved by extracting the predicted data from a spherical distribution of microphones to analyze the directivity of the sound emissions at BPF and harmonics. Figure 7(a) is reported as an example to understand how the bottom views of the hemispheres analyzed below are built (see for instance Figure 7(b)). Such bottom views are chosen since we are typically interested in controlling sound emissions propagating toward the ground rather than toward the sky.

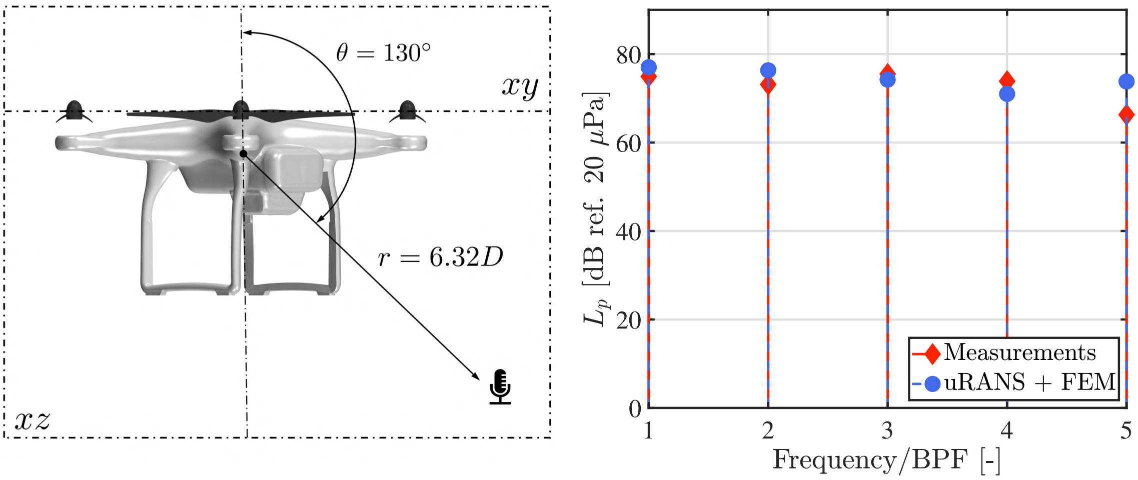

(a) (b)

Figure 3: (a) Same listener position adopted for the noise measurement of the DJI Phantom 3 Advanced in [13] is reported in the illustration. (b) Numerical results obtained in this work through the hybrid uRANS+FEM methodology are compared with the experimental ones measured in [13].

4.2 Tip-on-tip interaction

In this section we study the aerodynamic installation due to the tip-on-tip noise mechanism, to quantify the unsteady variations of the forces produced from this phenomenon. In order to compare these interaction effects, the velocity field of an isolated propeller (grid 1 in Section 2) is also simulated, as shown in Figure 4(a). One can notice the symmetry of the wake which is well evacuated toward the outlet of the computational domain. The flow upstream of the propeller appears symmetrical, limiting the influence of unsteady-loading effects, as discussed in Section 1. Figure 5(a) shows the coherent evolution of the slipstream produced at the isolated blade tip, calculated using the Q-criterion with $q = 35\,000\,\mathrm{s}^{-2}$ (more details in [12]). On the isosurface the turbulent kinetic energy (TKE) is shown, which increases considerably both at the trailing edge and at the blade tip, and where the slipstream starts to break, about three radii downstream of the propeller. The undisturbed downstream evolution of the slipstream indicates that the unsteady-loading effects are weak, even though the advance ratio is zero in hover. A simulation including only the propellers and not the fuselage is performed, as visible in Figure 6(a). Here,

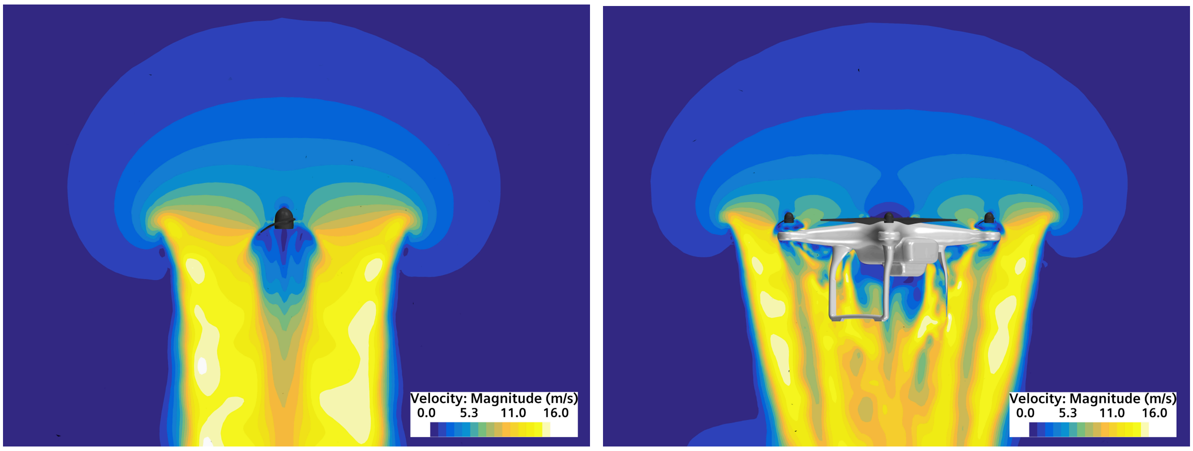

(a) (b)

Figure 4: Sections over the $(x, z)(y = 0)$ plane of the velocity magnitude fields for the isolated propeller (a) and for the quadcopter (b).

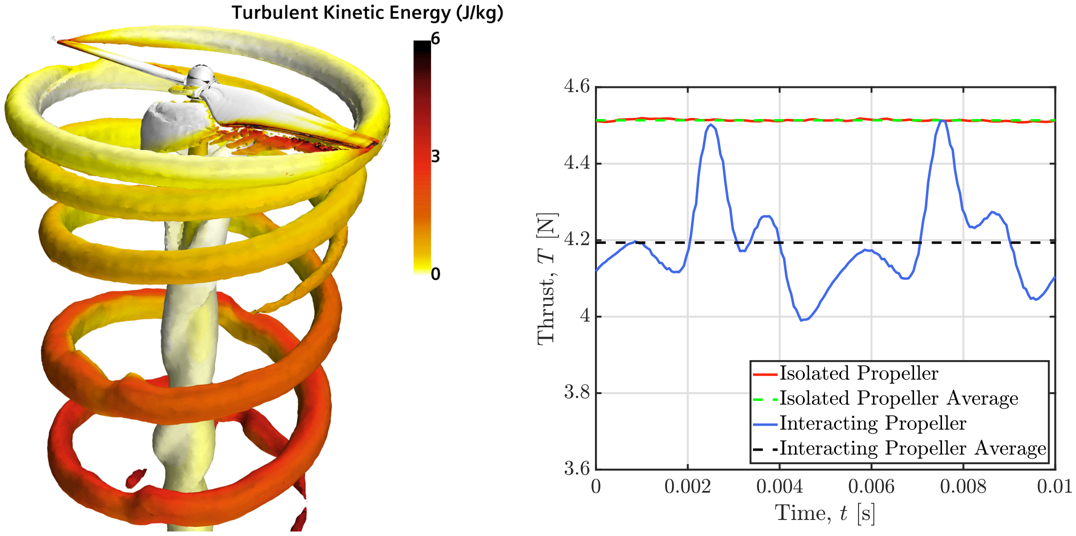

(a)

(b)

Figure 5: (a) Tip slipstream evolution of the isolated propeller. The isosurface is calculated through the Q-criterion with a value of $q = 35\,000\,\mathrm{s}^{-2}$ and colored by TKE. (b) Comparison between the thrust of the isolated propeller against the one of a propeller interacting with the other three (with no fuselage). In solid line, the instantaneous quantities are shown, whereas in dashed line the time-averaged ones are depicted.

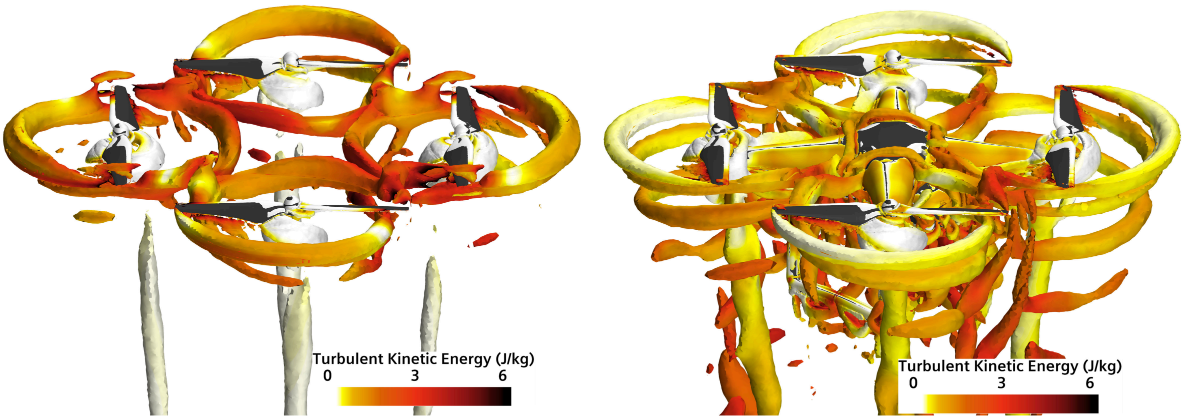

(a)

(b)

Figure 6: Isosurface obtained through the Q-criterion with a value of $q = 35\,000\,\mathrm{s}^{-2}$ and colored by TKE. In (a), the case with the four propellers is illustrated; in (b), the case with four propellers and fuselage.

we display the isosurface calculated through the Q-criterion with a value of $q = 35\,000\,\mathrm{s}^{-2}$, colored by TKE. It is observed that the interactions between blade tips are so strong that the slipstreams of each rotor are unable to evolve in the flow direction, differently from the ones of the isolated propeller shown in Figure 5(a). In the former case, where TKE increases there is an interaction between the blade tips that dissolves the coherence of the slipstreams. The consequence of these strong interactions results in a high degree of unsteadiness in the surroundings of the propellers. This translates into large fluctuations of the aerodynamic forces acting on each rotor, as can be observed in Figure 5(b). Here, the thrust of the propeller interacting with the others shows major fluctuations of 7% with respect to its average value. The latter is reduced by 7% when compared to the average value of the thrust in the isolated case. The consequence is that the aerodynamic interaction between the tips of the blades is not only a source of unsteady loading noise but is also deleterious on the aerodynamic performance. Thrust reduction due to the proximity of one rotor to the others is documented in the literature, for example by de Vries *et al.* [8], who found local loading variations of 5% – 10% when the proximity between adjacent propellers is minimized. Figure 7(b) illustrates the bottom views of the sound directivity hemispheres introduced in Figure 7(a). These are

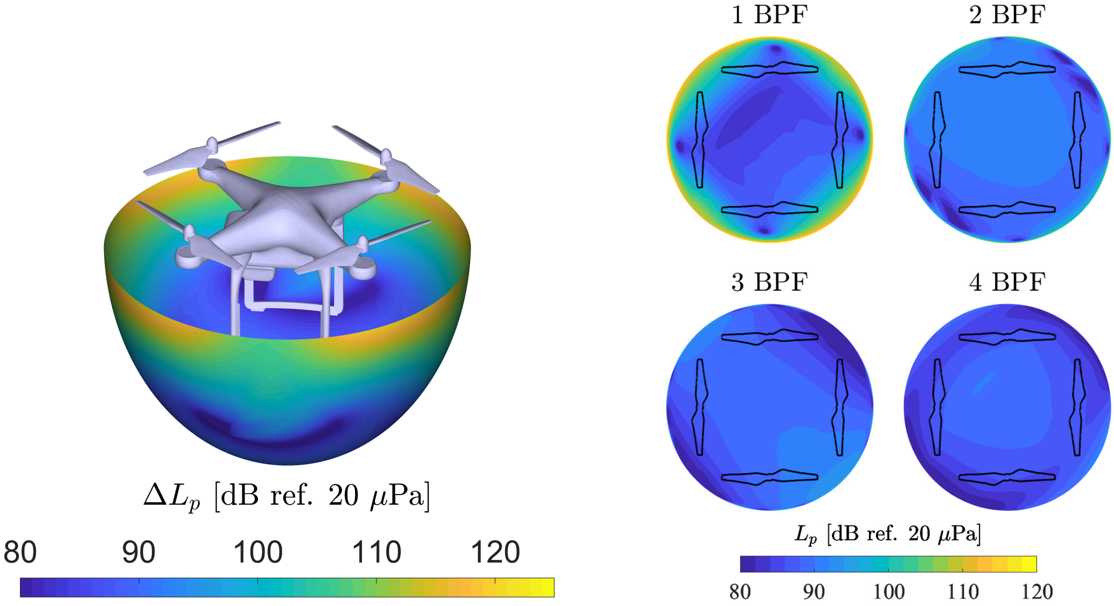

(a) (b)

Figure 7: (a) SPL concerning the first BPF of the four propellers and fuselage. It is plotted on a hemisphere with the center defined as in Figure 3(a), and a radial distance of $r = 1.1D$ to capture the near fields effects of the quadcopter noise emissions. (b) Bottom views of L_p directivity plots concerning the first four BPFs for the case with four propellers and no fuselage. The hemispheres here illustrated are created as the example given in Figure 7(a).

presented for L_p at the first four BPFs involving the simulated case with only four propellers and no fuselage. The sound directivity is not homogeneous at all considered BPFs. In particular, the sound is emitted mainly in the plane of the rotors at the first two BPFs, showing a difference between this area and the central one of $15\,\mathrm{dB}$. Only the first BPF exhibits also relevant emission zones extending to the surroundings of the blades' tips.

4.3 Tip-on-strut interaction

The aim is here to quantify the aerodynamic installation effects due to the presence of the fuselage and its supporting struts just below the propellers. The uRANS simulation concerning the quadcopter case, i.e., including propellers and fuselage, is shown in Figure 4(b). We observe that, unlike the isolated propeller case, the rotor inflow conditions are no longer axisymmetric; each rotor must interact with the presence of the other three and the downstream fuselage. Consequently, aerodynamic installation effects dominate for this case, due to the azimuthally non-uniform conditions affecting the unsteady forces of each rotor. In Figure 6(b), the Q-criterion with a $q = 35\,000\,\mathrm{s}^{-2}$ value is used to reveal the coherent structures colored by TKE. Like the case with only four propellers, we observe the interaction zones between the tips of the blades, marked by an increase of TKE. These interactions tend to dissolve the slipstreams just downstream of the rotors. Interestingly, the slipstreams do not break immediately as in the four-propellers case but evolve for about three turns before dissolving. Like this case, tip-on-tip interactions enhance the unsteadiness in the surroundings of the propellers, which results in increased fluctuations of the unsteady aerodynamic forces on the rotor disks. Furthermore, in Figure 6(b), we notice an additional source of instability corresponding to the presence of the supporting struts of the quadcopter body. These deform the coherent structures highlighted by the Q-criterion because of the potential distortion of the flow investing them.

In Figure 8(a), we evaluate the aerodynamic installation effects at the four analyzed BPFs, caused by the presence of the fuselage (without considering its scattering). The first BPF presents a directivity similar to that of the four-propellers case previously examined in Figure 7(b). The emissions occur mainly in the rotor plane, with a minimum in correspondence of the tips' interaction zones. For the subsequent BPFs, on the contrary, the maximum emission is located around the center of the fuselage. In particular, the third BPF shows a higher emissivity zone

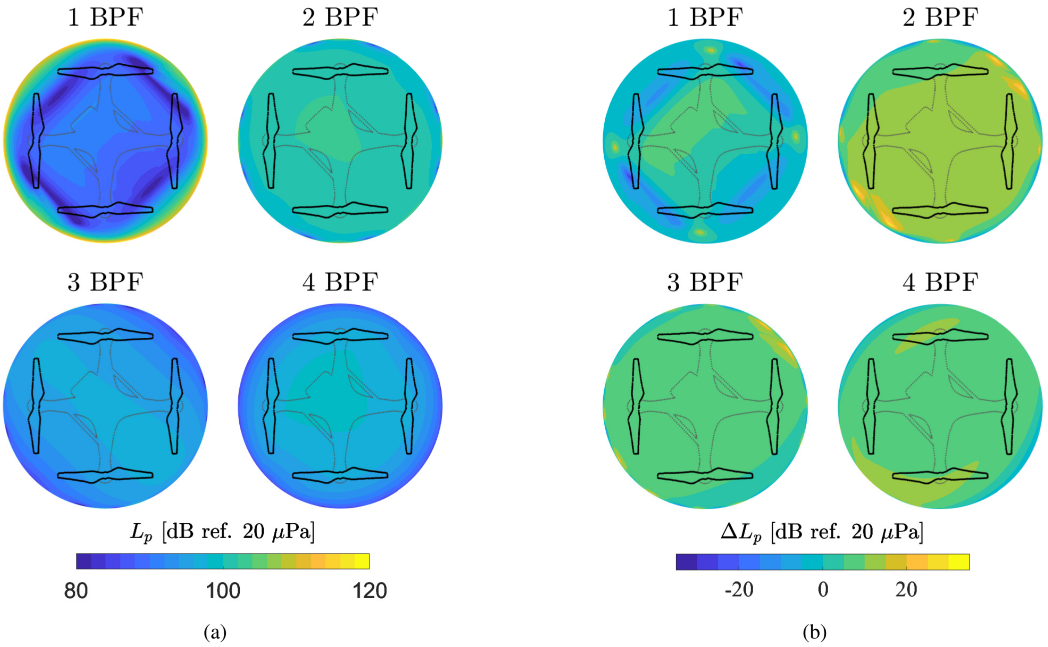

Figure 8: (a) Bottom views of SPL directivity plots concerning the first four BPFs for the case with four propellers and fuselage, without accounting for the scattering effects of the latter. (b) Bottom views of ΔL_p directivity plots concerning the first four BPFs comparing the case with four propellers and fuselage, without accounting for the scattering effects of the latter, to the case with four propellers and no fuselage. The hemispheres here illustrated are created as the example given in Figure 7(a).

parallel to the landing gear. It is interesting to observe in Figure 8(b) the difference expressed in ΔL_p between the case that considers the aerodynamic contribution of the fuselage and the one that does not. At the first BPF, the interaction zones between the tips emit more noise when the fuselage is not considered. However, at successive BPF harmonics, the case that considers the aerodynamic effects of the fuselage emits more in almost all directions, with a higher sound pressure level difference of at least $\Delta L_p = 5\,\mathrm{dB}$ in the central area of the quadcopter.

5 Conclusions

The work discussed above focused on the characterization of aerodynamic installation effects caused by tip-on-tip and tip-on-strut interactions, which have been reported in the literature to affect the sound directivity of drones. A hybrid methodology has been employed to predict the tonal sound emissions radiated by a commercial quadcopter in hover. This is achieved by coupling an unsteady RANS approach for simulating the motion field around the quadcopter with a FEM-based technique to calculate the acoustic wave propagation. The methodology has been validated by comparing the results with already existing acoustic measurements. A good agreement below $3.5\,\mathrm{dB}$ is obtained at the first four BPFs. Consequently, the developed low-order hybrid methodology works accurately to predict the tonal noise of a quadcopter and can be used in the future to study other UAV configurations or different flight conditions. The unsteady tip-on-tip and tip-on-strut interactions are shown to be dominant noise-generating mechanisms that drastically change the flow features compared to an isolated-propeller case. In particular, the tip-on-tip interaction, which is studied through the four propellers and no-fuselage simulation, reduces the average thrust of each propeller by 7%, while increasing its fluctuations by 7% compared to the isolated case. This is linked to the sudden breakdown of the coherent vortical structures that are instead observed to develop downstream of the propeller alone. Moreover, we highlighted that the emission directivity is not homogeneous. Indeed, the radiations in the plane of the rotors exceed $15\,\mathrm{dB}$ at the first two BPFs when compared to the radiations toward the ground. When the fuselage is included in the CFD simulation, another source of flow distortion is added between the blade tips and the supporting struts. It is worth noticing that the effect of the fuselage on the aerodynamic noise sources is to change greatly the emission directivity. When compared to the propellers-only simulation, we observed amplification in the direction toward the ground at the second BPF and successive harmonics of at least $5\,\mathrm{dB}$, reaching maximum differences of 30 dB. As a result, while examining the effects of UAV noise, for example in urban contexts, one must consider the aerodynamic installation effects as they drastically alter the sound directivity of these systems.

Acknowledgements

The authors acknowledge receiving funding from the European Union's Horizon 2020 research and innovation programme under grant agreement number 860103. Additionally, we thank Dr. Korcan Kucukcoskun of Siemens Digital Industries in Belgium for his in-depth suggestions on the numerical methods, as well as Mr. Carl Russell of NASA Ames Research Center in the United States for providing the DJI Phantom 3 Advanced geometry.

Declaration of competing interest

The authors state that they have no known competing financial interests or personal relationships that could have influenced the research presented in this study.

References

[1] Phantom 3 Advanced. `https://www.dji.com/be/phantom-3-adv`, Accessed: 2022-01-12.

[2] Ed. Alvarado. 237 ways drone applications revolutionize business. *Drone Industry Insights*, Retrieved 11 May 2021.

[3] Hadrien Bériot and Axel Modave. An automatic perfectly matched layer for acoustic finite element simulations in convex domains of general shape. *International Journal for Numerical Methods in Engineering*, 122(5):1239–1261, 2021.

[4] L. Cary and J. Coyne. Icao unmanned aircraft systems (uas), circular 328. *2011-2012 UAS Yearbook - UAS: The Global Perspective*, Blyenburgh & Co. pp. 112–115.

[5] Damiano Casalino, Wouter C. van der Velden, and Gianluca Romani. Community noise of urban air transportation vehicles. In *AIAA Scitech 2019 Forum*. American Institute of Aeronautics and Astronautics, 2019.

[6] Damiano Casalino, Wouter C. van der Velden, Gianluca Romani, and Ignacio Gonzalez-Martino. Aeroacoustic analysis of urban air operations using the LB/VLES method. In *25th AIAA/CEAS Aeroacoustics Conference*. American Institute of Aeronautics and Astronautics, 2019.

[7] Talib Dbouk and Dimitris Drikakis. Quadcopter drones swarm aeroacoustics. *Physics of Fluids*, 33(5):057112, 2021.

[8] Reynard de Vries, Nando van Arnhem, Tomas Sinnige, Roelof Vos, and Leo L.M. Veldhuis. Aerodynamic interaction between propellers of a distributed-propulsion system in forward flight. *Aerospace Science and Technology*, 118:107009, November 2021.

[9] J. E. Ffowcs Williams and D. L. Hawkings. Sound Generation by Turbulence and Surfaces in Arbitrary Motion. *Philosophical Transactions of the Royal Society of London. Series A, Mathematical and Physical Sciences*, 264(1151):321–342, 1969.

[10] M.E. Goldstein. *Aeroacoustics*. Advanced book program. McGraw-Hill International Book Company, 1976. ISBN: 978-0-07-023685-1.

[11] Qiwei Guo, Yaozong Zhu, Yu Tang, Chaojun Hou, Yong He, Jiajun Zhuang, Youliang Zheng, and Shaoming Luo. CFD simulation and experimental verification of the spatial and temporal distributions of the downwash airflow of a quad-rotor agricultural uav in hover. *Computers and Electronics in Agriculture*, 172:105343, 2020.

[12] J. Hunt, Alan Wray, and Parviz Moin. Eddies, streams, and convergence zones in turbulent flows. *Studying Turbulence Using Numerical Simulation Databases*, -1:193–208, 11 1988.

[13] Nanyaporn Intaratep, William N. Alexander, William J. Devenport, Sheryl M. Grace, and Amanda Dropkin. Experimental Study of Quadcopter Acoustics and Performance at Static Thrust Conditions. In *22nd AIAA/CEAS Aeroacoustics Conference*, Lyon, France, May 2016. American Institute of Aeronautics and Astronautics.

[14] Idris Jeelani and Masoud Gheisari. Safety challenges of uav integration in construction: Conceptual analysis and future research roadmap. *Safety Science*, 144:105473, 2021.

[15] S. Kesselman. The first 1,000 commercial uas exemptions. *Association for Unmanned Vehicle Systems International*, 2016.

[16] Yan Li and Chunlu Liu. Applications of multirotor drone technologies in construction management. *International Journal of Construction Management*, 19(5):401–412, 2019.

[17] Florian R. Menter. Two-equation eddy-viscosity turbulence models for engineering applications. *AIAA Journal*, 32:1598–1605, 1994.

[18] M. Roger. *Aeroacoustics of installed propellers*. Number 2019-02 in von Karman Institute Lecture Series. von Karman Institute for Fluid Dynamics, 2019.

[19] Michel Roger and Korcan Kucukcoskun. Near-and-far field modeling of advanced tail-rotor noise using source-mode expansions. *Journal of Sound and Vibration*, 453:328–354, August 2019.

[20] Gianluca Romani, Edoardo Grande, Francesco Avallone, Daniele Ragni, and Damiano Casalino. Performance and noise prediction of low-Reynolds number propellers using the Lattice-Boltzmann method. *Aerospace Science and Technology*, page 107086, 2021.

[21] Carl Russell, Jaewoo Jung, Gina Willink, and Brett Glasner. Wind tunnel and hover performance test results for multicopter UAS vehicle. In *AHS* 72^{nd} *Annual Forum*, West Palm Beach, FL, USA, May 2016.

[22] Herrmann Schlichting and Klaus Gersten. *Boundary-layer theory*. Springer, 2017.

[23] Siemens. *Simcenter Nastran Acoustics User's Guide (version 2022.1)*, 2022.

[24] P.R Spalart. Strategies for turbulence modelling and simulations. *International Journal of Heat and Fluid Flow*, 21(3):252–263, 2000.

[25] Antonio J. Torija and Charlotte Clark. A psychoacoustic approach to building knowledge about human response to noise of unmanned aerial vehicles. *International Journal of Environmental Research and Public Health*, 18(2), 2021.

[26] Simon Watkins, Jane Burry, Abdulghani Mohamed, Matthew Marino, Samuel Prudden, Alex Fisher, Nicola Kloet, Timothy Jakobi, and Reece Clothier. Ten questions concerning the use of drones in urban environments. *Building and Environment*, 167:106458, 2020.

[27] Seokkwan Yoon, Patricia Ventura Diaz, D Douglas Boyd Jr, William M Chan, and Theodore R Colin. Computational aerodynamic modeling of small quadcopter vehicles. page 16, AHS 73^{rd} Annual Forum, 2017.

[28] Seokkwan Yoon, Thomas H Pulliam, and Neal M Chaderjian. Simulations of xv-15 rotor flows in hover using overflow. In *fifth decennial AHS aeromechanics specialists' conference, San Francisco, CA*, pages 22–24, 2014.

[29] Alessandro Zarri, Julien Christophe, Stéphane Moreau, and Christophe Schram. Influence of Swept Blades on Low-Order Acoustic Prediction for Axial Fans. *Acoustics*, 2(4):812–832, November 2020.

[30] Alessandro Zarri, Julien Christophe, and Christophe F. Schram. Low-Order Aeroacoustic Prediction of Low-Speed Axial Fan Noise. In *25th AIAA/CEAS Aeroacoustics Conference*, Delft, The Netherlands, May 2019. American Institute of Aeronautics and Astronautics.

[31] Nikolas S. Zawodny and Douglas D. Boyd. Investigation of rotor–airframe interaction noise associated with small-scale rotary-wing unmanned aircraft systems. 65(1):1–17, Journal of the American Helicopter Society, 2020.